PNAS RESEARCH ARTICLE | EARTH, ATMOSPHERIC, AND PLANETARY SCIENCES

Suborbital- and millennial-scale monsoon variability during Pleistocene interglacials

Youbin Sun[a,1], Ting Wang[a,b], Qiuzhen Yin[c], Steven C. Clemens[d], Xingxing Liu[a], Li Ai[a], Zhipeng Wu[c], Xiaoke Qiang[a], Xulong Wang[a], Hong Chang[a], Yougui Song[a], Hendrik Vogel[e], John Dodson[a,f], Andre Berger[c], and Zhisheng An[a,g,1]

Affiliations are included on p. 7.

Contributed by Zhisheng An; received December 16, 2024; accepted May 5, 2025; reviewed by Julie Brigham-Grette and Jule Xiao

Observational and modeling results show that the frequency and amplitude of extreme climatic events have increased significantly in the context of global warming. However, whether abrupt climate changes intensified during past warm periods remains poorly constrained due to the lack of high-resolution geological records. Here, we report a 512-m predominantly lacustrine sedimentary record from the Weihe Basin (North China), revealing that lake levels fluctuated significantly on suborbital (half- and quarter-precession) and millennial timescales over the last 2 Ma. Grain-size results reveal that magnitudes of rapid lake level fluctuations increased dramatically during Pleistocene interglacials, differing from glacial amplification of abrupt climate events recorded in North Atlantic marine sediments. Model results indicate that summer insolation maxima in low-latitude region of both hemispheres can lead to intensified monsoon precipitation in East Asia. Our proxy-model comparison highlights the importance of low-latitude bihemispheric insolation maxima in driving millennial-scale hydroclimatic variability in a warming future.

East Asian monsoon | Suborbital- and millennial-scale variability | Pleistocene interglacials | Low-latitude insolation forcing

Significance

Marine and ice-core records demonstrate that Heinrich events and DO cycles were persistently significant during the Pleistocene glaciations. However, it remains unclear how abrupt climate events evolved during past warm periods and whether the driving mechanisms differ between glacial and interglacial boundary conditions. Our centennial-resolution grain size proxies from a 512-m lacustrine-dominated core reveal that monsoon-induced lake level in the Weihe Basin fluctuated dramatically on suborbital and millennial timescales during Pleistocene interglacials. We propose that rapid monsoon changes during Pleistocene interglacials could be triggered by bihemispheric maximum insolation over the low-latitude oceans. Our unique record provides a natural analog for predicting the future trajectory of periodic extreme climate events.

Meteorological observations show that extreme flood and drought events occurred frequently across the world in recent decades, posing threats to food security and natural sustainability (1, 2). Historical documents and speleothem records show that extreme droughts not only cause social turmoil and ethnic disputes but even lead to the decline in civilizations and fall of dynasties (3, 4). Droughts, depending on their rate of occurrence and persistence, include flash-droughts occurring at subseasonal scales and megadroughts lasting for 100 y or longer (5). Multimodel projections show that the frequency and intensity of extreme drought events will increase under global warming (6, 7). Extreme droughts primarily originate from internal climate variability, such as El Niño-Southern Oscillation (ENSO) and Pacific decadal oscillation (8, 9). Human-induced climate change has exacerbated the concurrency of global extreme events (10). Among them, the ENSO appears to be the main driver of concurrent droughts occurring in global monsoon-affected regions (11).

In the densely populated Asia-Pacific region, the monsoon-induced hydrological cycles play a decisive role in driving flood and drought disasters (12). Oxygen isotopic records from corals and tree rings have revealed that ENSO can affect centennial- and decadal-scale hydroclimate variability in the Asia-Pacific region during the last millennia (13, 14). Modeling results suggest that coevolution between ENSO and monsoons is mainly linked through tropical oceanic processes (15) and jointly influenced by both natural and anthropogenic factors (16, 17). Proxy records from the South China Sea and the western equatorial Pacific reveal that low-latitude oceanic processes also played a key role in driving multiscale monsoon variability (18, 19). However, it remains unclear how abrupt monsoon changes evolved in past warm periods and whether the driving mechanisms differ between glacial and interglacial conditions. Therefore, high-resolution Pleistocene proxy records are crucial for addressing the role of low-latitude processes in driving suborbital- and millennial-scale monsoon variability.

In this study, a 512-m core was retrieved from Huxian (HX) located in the Weihe Basin at about 35 °N (North China) to address the characteristics and mechanisms of monsoon-induced hydroclimate variability during the Pleistocene. Magnetostratigraphic and lithostratigraphic results indicate that the HX core spans the past 2 million year (Ma) and the clay (<8 μm) content of the HX core is very sensitive to monsoon-induced lake level fluctuations. Clay content of the HX core demonstrates persistent and dramatic lake level fluctuations at suborbital and millennial timescales during the Pleistocene interglacial

Author contributions: Y. Sun and Z.A. designed research; Y. Sun, T.W., Q.Y., X.L., and Z.A. performed research; Y. Sun, T.W., Q.Y., S.C.C., X.L., L.A., Z.W., X.Q., X.W., H.C., Y. Song, and Z.A. analyzed data; and all authors wrote the paper.

Reviewers: J.B.-G., University of Massachusetts Amherst Graduate School; and J.X., Institute of Geology and Geophysics, Chinese Academy of Sciences.

The authors declare no competing interest.

[1]To whom correspondence may be addressed. Email: sunyb@ieecas.cn or anzs@loess.llqg.ac.cn.

This article contains supporting information online at https://www.pnas.org/lookup/suppl/doi:10.1073/pnas.2426353122/-/DCSupplemental.

Published June 2, 2025.

periods, in stark contrast to the glacial amplification of abrupt climate events recorded in the high-latitude North Atlantic sediments (20, 21). Differing from the widely accepted high-latitude forcing of abrupt climate change, we propose that low-latitude insolation forcing also played a critical role in driving suborbital- and millennial-scale monsoon variability particularly during warm interglacials.

Results

Setting and Drilling. The Weihe Basin is bordered by the Qinling Mountains to the south and the Chinese Loess Plateau to the north (Fig. 1). This region is immensely affected by the East Asian monsoon, with distinctive seasonal changes in temperature and precipitation. Previous geophysical survey and borehole data reveal that two deposition centers are located at the eastern and western part of the Weihe Basin, accumulating over 7,500-m-thick eolian-lacustrine deposits (22). Investigation of outcrops exposed along the southern margin of the Weihe Basin indicates that the sedimentary environment in this region experienced a stepwise evolution from warm-dry to warm-wet and then to cold-dry phases since the Middle Eocene (23). Sedimentological and geochemical results of the Luyanghu Core retrieved from the northern margin of the eastern depocenter show rapid dry-wet fluctuations of the depositional environment over the past 1 Ma (24).

Two parallel cores (HX-A: 512 m, HX-B: 110 m) were retrieved in the western depocenter near Huxian county (Fig. 1), with a composite core recovery rate of 98.3% (*SI Appendix*, Fig. S1*A*). Resistivity data obtained from down-hole logging reflect changes in grain size and associated porosity, and thus are sensitive to monsoon-induced changes in the sedimentary environment of the Weihe Basin (*SI Appendix*, Fig. S1*B*). Reflectance spectroscopy and magnetic susceptibility were measured at 2-cm resolution on the split core sections. Powder samples were taken at 2-cm intervals from the split cores for grain-size measurement after removal of organic matter and carbonates. Variations of color and grain size proxies indicate that the HX core consists of reworked loess deposits in the upper portion (0 to 25 m) and alternating lacustrine clay and deltaic sand layers in the lower part (*SI Appendix*, Fig. S1 *C*–*J*). Sedimentary facies can be well distinguished by core photography and grain size variations (Fig. 2 *D*–*F* and *SI Appendix*, Fig. S2), including reworked eolian deposits, littoral-to-shallow lake, and deltaic sediments.

Grain Size Proxies and Chronology. Grain size parameters of lake sediments in East Asia have been widely used to infer lake level change (28, 29), because lake shrinkage and expansion can result in different transportation of detrital sediments from the lake catchment to the coring site. Variations of HX grain size parameters can be categorized into two groups. One group (mean grain size, sorting coefficient, and sand content, *SI Appendix*, Fig. S1 *F*–*H*) is characterized by large-amplitude fluctuations during glacials, and the other group shows distinctive glacial–interglacial and fine-scale oscillations during both glacials and interglacials (i.e. silt and clay contents, *SI Appendix*, Fig. S1 *I* and *J*). During interglacials, sediments are mostly silty clay (shallow lake subfacies, *SI Appendix*, Fig. S2*B*) interbedded with grayish thin sandy silt layers (littoral lake subfacies, *SI Appendix*, Fig. S2*C*), reflecting frequent lake level fluctuations. During glacial periods, sedimentary successions are predominantly composed of grayish sand-bearing layers (deltaic facies, *SI Appendix*, Fig. S2*D*) due to persisting low lake levels. We adopt the clay content as a sensitive indicator of lake level fluctuation, because it can capture full amplitude of suborbital and millennial variability during both glacial and interglaical periods.

Paleomagnetic samples were taken from the HX-A core at 1-m intervals for alternating field and thermal demagnetization analyses (*Materials and Methods* and *SI Appendix*, Fig. S3). The results show that four geomagnetic reversals occur at depths of 173.6, 216.6, 236, and 449.7 m (Fig. 2 *A*–*C*), corresponding to the boundaries of Brunhes/Matuyama, top and bottom Jaramillo, and top Oldvuai (26), respectively. Two short-term negative anomalies are observed during the Brunhes epoch, and 7 to 10 positive excursions are recorded in the Matuyama epoch as inferred from

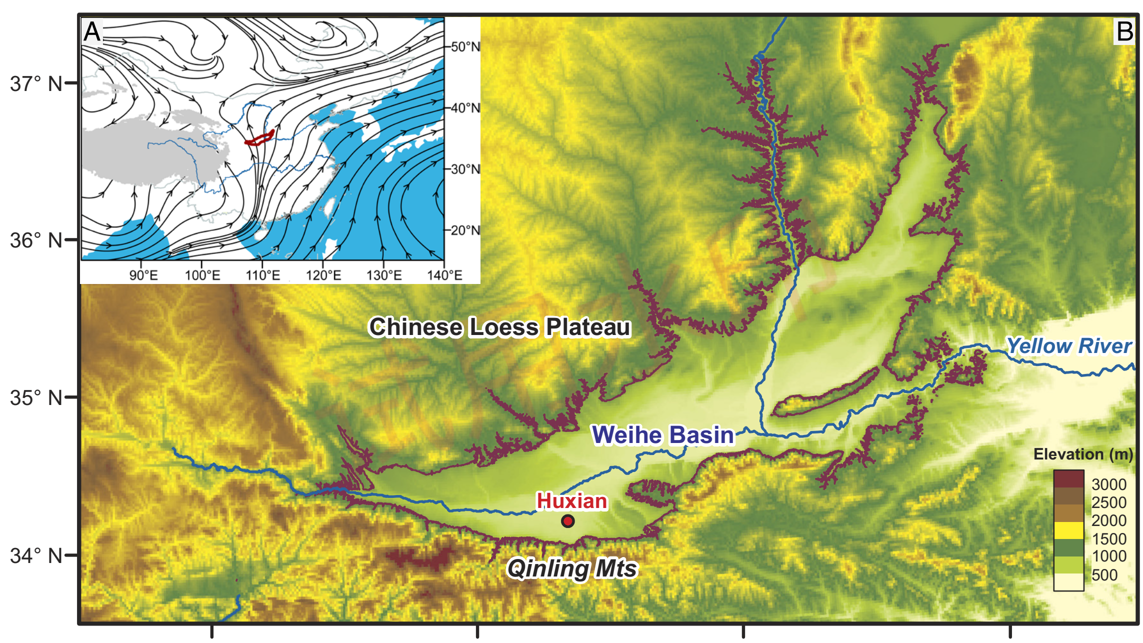

Fig. 1. Location of Huxian (HX) core in the Weihe Basin. (*A*) Weihe Basin is sensitive to East Asian summer monsoon as shown by mean 850 hPa streamline during summer season from atmospheric research reanalysis data during 1971–2000 (25); (*B*) Brown line denotes the 800-m contour line as the boundary of the Weihe Basin.

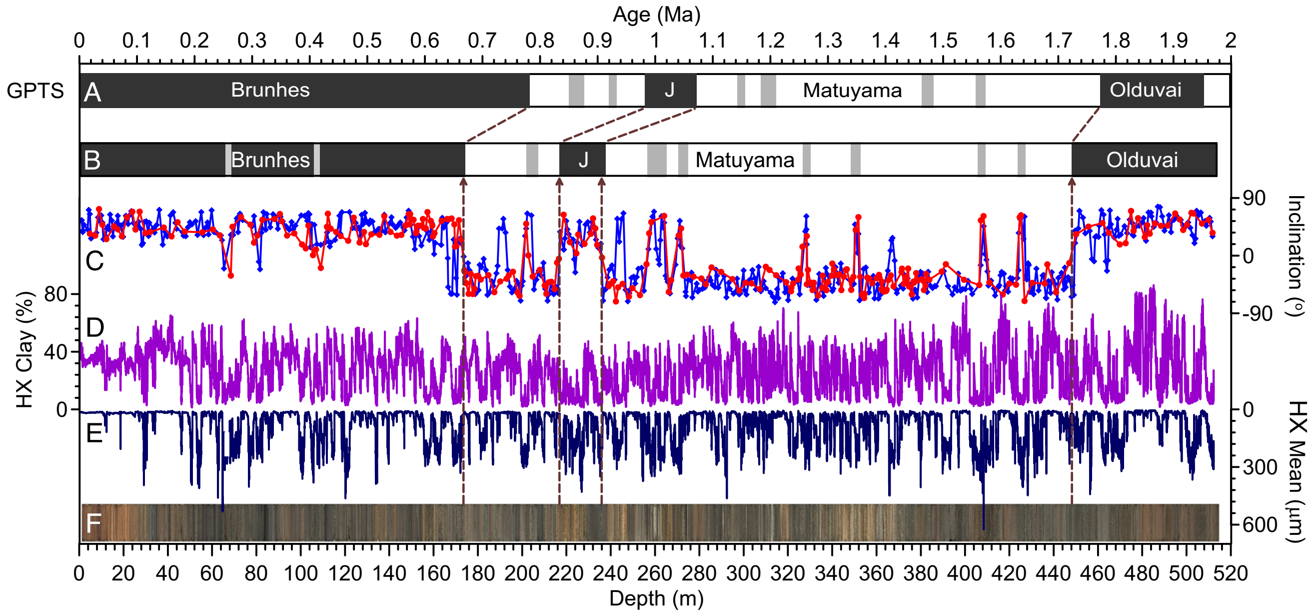

Fig. 2. Magnetostratigraphy and grain size results of the HX core. (*A*) Global polarity timescale (GPTS) and Quaternary geomagnetic excursions (26, 27); (*B*) Magenotstratigraphy of the HX core inferred from (*C*) inclination results of thermal (red) and alternating-filed (blue) demagnetization; (*D*) Clay content; (*E*) Mean grain size of the HX core; (*F*) Core photos. Dashed lines denote major paleomagnetic reversals.

thermal and alternating demagnetization results, respectively. The timing of these excursions has been well dated in volcanic and sedimentary archives (27). Estimated from the paleomagnetic results, the basal age of the HX core is younger than 1.95 Ma (i.e., the timing of bottom Olduvai subchron) and the average sedimentation rate is ~26 cm/ky for the HX core.

The evolutionary power spectrum of the logging resistivity data on depth scale reveals two dominant periods at 10.8-m and 4.7-m (*SI Appendix*, Fig. S4*A*). An initial paleomagnetic age model was established by linear interpolation of four time controls from the geomagnetic reversals, and two dominant periodicities became evident at 44- and 19-ky in the wavelet spectrum (*SI Appendix*, Fig. S4*B*). The age model was further refined by matching rapid changes in logging resistivity data to glacial/interglacial transitions of the benthic $\delta^{18}O$ stack (30, 31) (*SI Appendix*, Fig. S5). Based on the finely tuned age model, the resistivity variation shows a distinctive periodic transition from 41 to 100-ky cycles during the middle Pleistocene (1.2 to 0.7 Ma) (*SI Appendix*, Fig. S4*C*). Glacial–interglacial variations of the HX mean grain size and resistivity show high correlation with the benthic $\delta^{18}O$ stack (*SI Appendix*, Fig. S5).

Discussion

Suborbital- and Millennial-Scale Climate Variability. HX clay content exhibits significant glacial–interglacial fluctuations, superimposed by distinctive suborbital- and millennial-scale variability (Fig. 3*D*). Ensemble Empirical Mode Decomposition results of the HX clay content show six intrinsic mode functions (IMFs) related to orbital, suborbital, and millennial variability (*SI Appendix*, Fig. S6*A*). Wavelet spectra of HX clay content and six IMFs reveals distinct periodicities at ~100-, 41-, 21-, 19-, 10.5-ky, 5.5-, and 2.8-ky (*SI Appendix*, Fig. S6*B*). Relative contributions of six IMFs ranging from 9.0% to 21.1% reveal that the precession (21-ky) and half-precession (10.5-ky) cycles are stronger than the other orbital and millennial components. Notably, the mid-Pleistocene transition (MPT) in our HX clay content is characterized by intensification of the 100-ky cycle around 1.2 Ma, while both the 41- and 21-ky cycles were persistent over the last 2 Ma. Moreover, magnitudes of suborbital and millennial variability were stronger before the MPT (2 to 1.25 Ma) than afterward, differing from stepwise intensified millennial climate variability inferred from North Atlantic proxy records (32).

HX clay content exhibits significant glacial–interglacial fluctuations similar to proxies from other lake records in East Asia. While proxies from three Pleistocene paleolake records exhibit similar glacial–interglacial fluctuations (34–36), suborbital- to millennial-scale fluctuations are very distinctive in the pollen record of the Zoige basin (Fig. 3*C*) and the magnetic susceptibility of lake El'gygytgyn (Fig. 3*E*). Proxy records from a Maar lake in southern China also exhibit strong precession and half-precession cycles of East Asian summer monsoon variability (37). High-frequency (<12-ky) components of three lake-based proxies all display distinctive half- and quarter-precession cycles (*SI Appendix*, Fig. S7). By contrast, IRD records from North Atlantic sediments reveal that abrupt cooling events were particularly evident during glacial periods (21, 38) (Fig. 3*F*). Unlike glacial amplification of abrupt climate events from the North Atlantic (20, 21), our HX clay content shows more sustained suborbital- and millennial-scale monsoon oscillations during Pleistocene interglacials.

Variation of HX clay content reflects that dramatic dry/wet fluctuations were persistent during Pleistocene interglacials, but characterized by different magnitude and duration before and after the MPT (Fig. 4*B*). After the MPT, interglacial periods [e.g., marine isotope stages (MIS) 5, 7, 9, 11, 13, and 15] last about 30 to 60 ky and comprise 3 to 6 dry events with an average periodicity of 5 to 10 ky. During the MPT, abrupt monsoon events are characterized by small amplitude fluctuations relative to those in other interglacials, while the numbers vary between 2 and 4 during MIS 17 to 37. Prior to the MPT, while interglacial durations shortened to 20 to 30 ky, more dramatic lake level fluctuations lasting for several hundred years were well documented. Both the frequency and amplitude of abrupt monsoon events before the MPT were

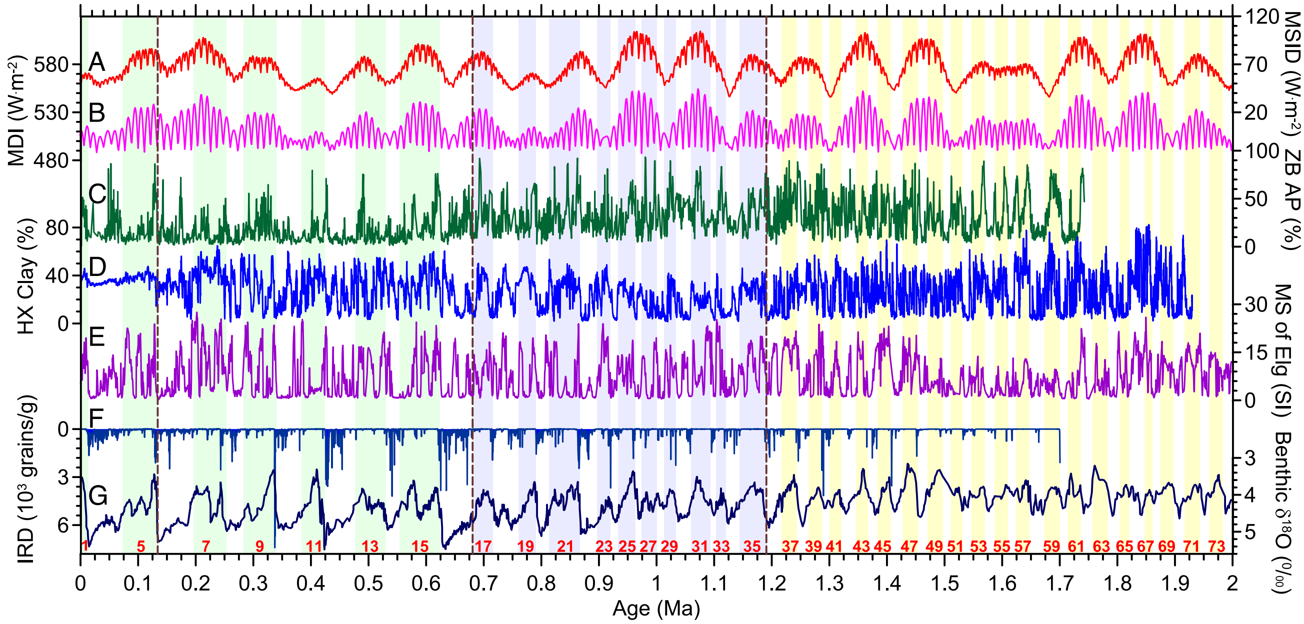

Fig. 3. Comparison of HX clay content with marine, lake, and insolation records. (*A*) Equatorial maximal seasonal insolation difference (MSID) and (*B*) Maximal daily insolation (MDI) at 30 °N and 30 °S (33); (*C*) Aboreal pollen (AP) content in the Zoige Basin (ZB) (34); (*D*) Clay content of HX core; (*E*) Magnetic susceptibility (MS) of lake El'gygytgyn (Elg) (35); (*F*) Ice-rafted debris (IRD) content of Site 983 (21); (*G*) Benthic $\delta^{18}O$ stack (30). Light yellow, blue, and green bars denote interglacials before, during, and after the MPT, respectively.

higher than those during the post-MPT interglacials. Our record differs from high-latitude records which show relatively stable interglacial climate conditions as evidenced by less cooling events [Fig. 3*F*, (21, 38, 39)] and weak millennial climate variability [Fig. 4*A*, (32, 40, 41)], suggesting that interglacial monsoon instability was unlikely forced by high-latitude processes.

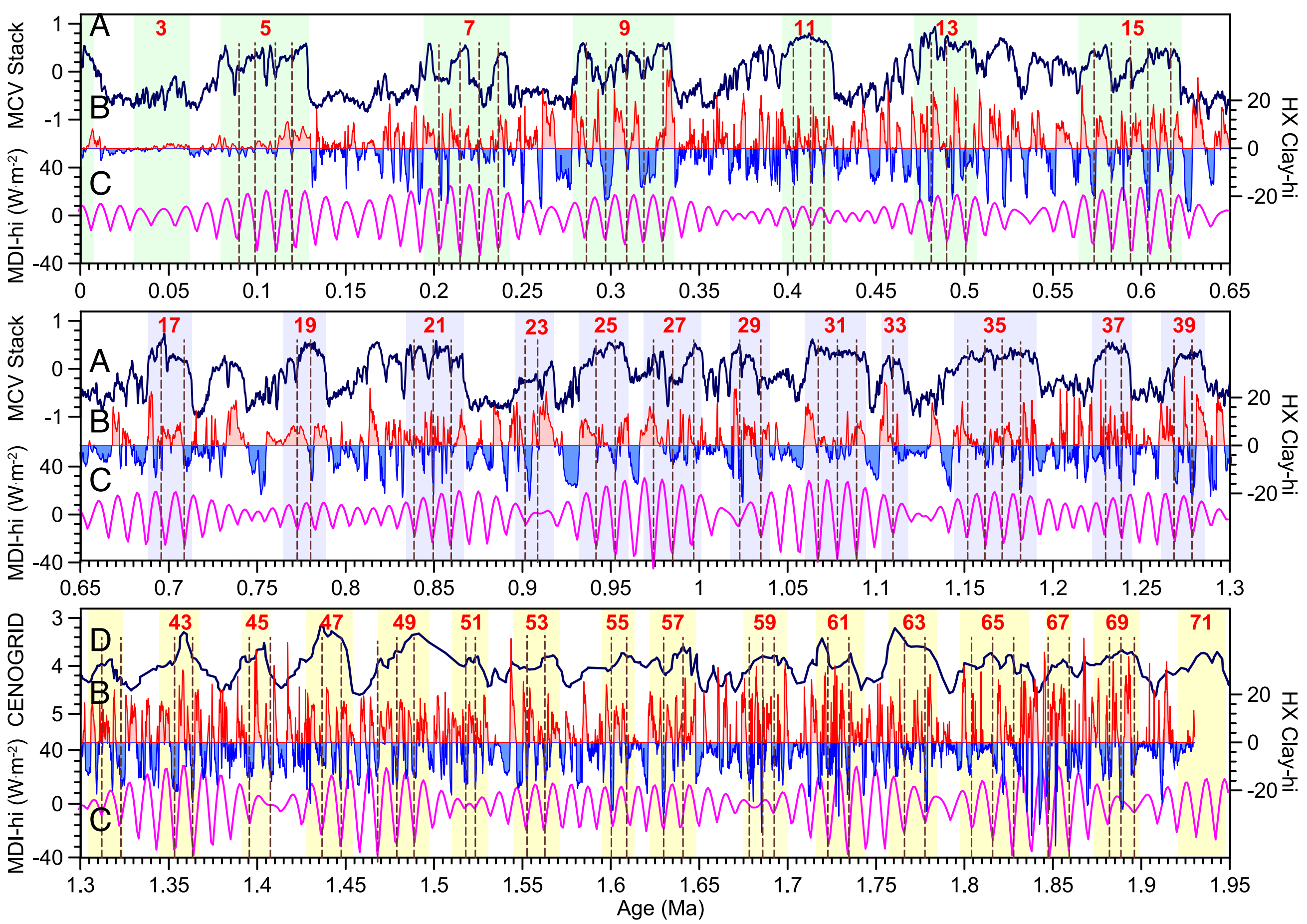

Fig. 4. Abrupt climate changes over the last 2 Ma. (*A*) Millennial climate variability (MCV) (40); (*B*) Strong (red) and weak (blue) monsoon events inferred from high-frequency component of HX clay content; (*C*) High-frequency (<12 ky) signal of bihemispheric maximal daily insolation (MDI-hi) at 30 °N and 30 °S (33); (*D*) Benthic $\delta^{18}O$ stack for 1.3 to 1.96 Ma (30). Light yellow, blue, and green bars denote interglacials before, during, and after the MPT, respectively. Dashed lines indicate that low MDI values roughly correspond to weak monsoon events.

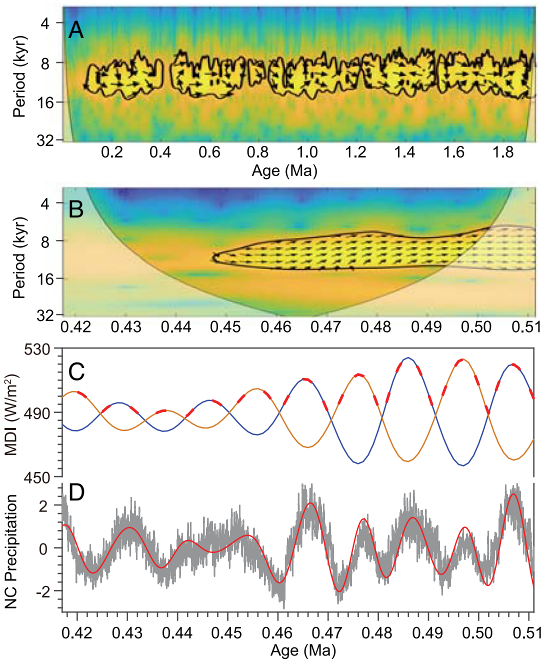

Fig. 5. Correlation of half-precession signals in HX clay content, MDI, and simulated summer precipitation. (*A*) Cross wavelet spectra between the 8 to 12 ky component of the HX clay content and MDI at 30 °N and 30 °S; (*B*) same as (*A*) but for the 8 to 12 ky component of the simulated summer precipitation in North China (NC, 30 to 40 °N, 105 to 120 °E); (*C*) MDI: blue (yellow) line is June (December) insolation at 30 °N (30 °S) (33); (*D*) High-frequency signal of simulated summer precipitation in North China (the gray line is the <12 ky high-pass filtering result with standardized 100-y running mean, and the red line is the 8 to 12 ky band-pass filtering component).

Low-Latitude Forcing of Suborbital Climate Change. Characteristics and mechanisms of rapid climate changes have been addressed intensively from proxy and modeling perspectives (42) and could be triggered by external insolation forcing and internal feedbacks under both glacial (43) and interglacial conditions (44). As far as low-latitude insolation is concerned (33, 45), a notable feature is the half-precession cycles in the equatorial insolation maxima and quarter-precession cycles in the maximum amplitude of the seasonal insolation cycle (Fig. 3*A* and *SI Appendix*, Fig. S7). This is due to the fact that the Sun passes through the equatorial region twice a year with insolation maxima occurring during spring and autumn equinoxes (33). While the high-frequency variability of HX clay content is strongly coherent with the maximum seasonal insolation difference (MSID) at half- and quarter-precession bands (*SI Appendix*, Fig. S8), the phase relationship is unstable likely due to age model uncertainties. Meanwhile, bihemispheric maximum daily insolation (MDI) on summer solstice at 30 °N and on winter solstice at 30 °S show strong precession- and half-precession signals (Fig. 3*B* and *SI Appendix*, Fig. S7), which plays a key role in driving monsoon-related hydrological and sea surface temperature changes (46, 47).

High clay contents generally match with bihemispheric MDI particularly during Pleistocene interglacials (Fig. 4 *B* and *C*), confirming a potential link of suborbital-scale monsoon variability to low-latitude insolation forcing. Cross-wavelet analysis reveals that half-precession signal in HX clay content is strongly coherent with, and generally in-phase with the MDI throughout the past 2 Ma (Fig. 5*A*), indicating a significant influence of bihemispheric insolation maxima on suborbital-scale hydroclimatic changes. Low-latitude insolation forcing can be confirmed by the results of a transient simulation covering the MIS 13 to 12 (511 to 417 ky). The simulation was performed with the LOVECLIM model for several precession cycles to address the relationship between solar radiation and the East Asian monsoon precipitation (48). Similar to the half-precession monsoon revealed by the HX clay content, the simulated summer precipitation in north China also shows significant half-precession cycles (Fig. 4*D*). Moreover, the half-precession signal in the simulated summer precipitation has an in-phase relationship with MDI (Fig. 5 *B* and *C*), confirming the strong coupling between bihemispheric insolation maxima and half-precession monsoon variability.

As the heat and moisture engine of global monsoon change, the low-latitude oceans play a vital role as drivers of ocean-atmosphere convection as well as -water vapor transport toward mid-latitude continents (18). Both modern observations and model simulations indicate that global warming will result in increased sea surface temperature and heat capacity in the upper ocean over the equatorial region (49), consequently leading to an invigorated hydrological cycle with strong La Niña events and enhanced East Asian monsoon precipitation (50). Similar to the half-precession variability observed in HX clay content, sea surface temperature records from the tropical western Pacific exhibit suborbital-scale fluctuations related to bihemispheric maximum insolation in the low-latitude regions (48, 51). Proxy and model results reveal that low-latitude hydrological cycles are driven by two primary mechanisms: sensible heating by boreal summer insolation maxima and interhemispheric latent heating by austral summer insolation maxima (52). Strong monsoon circulation during boreal summer is driven by enhanced land–ocean thermal contrast and northward migration of the ITCZ (53), while strong monsoon circulations can also be driven by intensified cross-equatorial heat and moisture transport from the southern hemisphere during austral summer (54–56). Therefore, the low-latitude oceans could be an important medium to transmit the suborbital-scale signal of the low-latitude insolation forcing to the hydroclimate variability by the cross-equatorial thermal pull and pressure push hypothesis (36).

Future Implication of Monsoon Instability. Our investigation on past climate instability during warm interglacials could provide clues for future prediction. Sharing a similar low-eccentricity configuration with the current interglacial (MIS 1) (57, 58), the interglacial MIS 11 has been suggested as a natural analog for assessing future climate evolution of the current interglacial without human disturbance. Given the key role of bihemispheric MDI in suborbital- and millennial-scale monsoon variability, we align the bihemispheric MDI between MIS 11 and MIS 1 to address the future trend of monsoon instability (Fig. 6 *A* and *B*). Variation of HX clay content indicates that millennial-scale weak monsoon events became more predominant in the low MDI intervals (Fig. 6*C*). Comparison of MDI and HX clay content suggests that the summer monsoon will weaken dramatically after 2000 y. This weak monsoon period would last for 4 ky and contain three weak monsoon events, in contrast to the relatively stable interglacial climate at high latitudes [Fig. 6*D*, (39)]. Subsequently, the monsoon will recover to its full interglacial strength and last for 6 ky until another abrupt weakening (like events 9 to 11) occurs about 12000 y later.

Summary. Proxy records from the Weihe Basin reveal persistent suborbital- and millennial-scale monsoon variability over the past 2 Ma. Unlike relatively stable interglacial climate in high-latitude regions, our grain size records exhibit prominent suborbital- and millennial-scale fluctuations during the Pleistocene interglacials. Differing from high-latitude glacial amplification of abrupt climate changes, we emphasize that bihemispheric insolation impact on low-latitude oceanic processes (i.e., cross-equatorial heat and

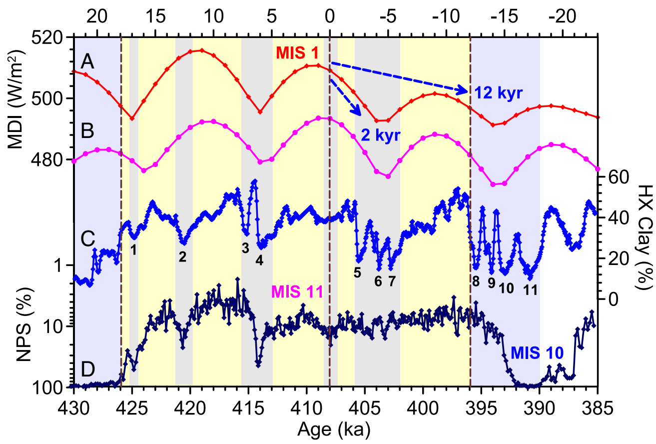

Fig. 6. Future implication of past climate changes during MIS 11. (*A* and *B*) MDI during MIS 1 (red) and MIS 11 (purple) (33); (*C*) HX clay content; (*D*) *N. Pachyderma* s. (NPS) content of ODP site 983 (39). Weak monsoon events are numbered in the HX clay content. Blue arrows denote the potential future trend and timing of millennial monsoon events under natural forcing.

moisture transports) could play a crucial role in driving suborbital- and millennial-scale hydroclimate variability during interglacial periods. Our proxy and model results reveal a strong coupling relationship between the bihemispheric maximum insolation, oceanic heat capacity, and monsoonal hydroclimate variability on suborbital and millennial timescales. These findings highlight that warming of low-latitude oceans associated with anthropogenic forcing will contribute to future hydroclimate instability. The predicted future trend toward more frequent extreme events by our results will be beneficial for proactively developing adaptation strategies to the risk of global change.

Materials and Methods

Drilling and Logging. The Weihe Basin is very sensitive to seasonal changes in temperature and precipitation, characterized by cold–dry winter and warm–humid summer. At present, the mean annual temperature is 12 to 14 °C, and mean annual precipitation is 500 to 700 mm. 55% of the annual precipitation falls during the summer monsoon-dominated season (June to September), which is sourced primarily from the tropical Indo-Pacific oceans. In 2019, two cores (HX-A and HX-B) were drilled at Huxian (34.13 °N, 108.72 °E, 400 m asl) in the western subsidence center, with core recovery rates of 96.9% and 92.5%, respectively (*SI Appendix*, Fig. S1*A*). The main hole (HX-A, 512 m) was logged by the PSJ-1 digital logging tool at 5-cm interval with a velocity of 10 m/min. The logging parameters include resistivity and natural gamma radiation. The logging resistivity parameter is adopted to compare to mean grain size of the two holes for depth correction, because coarse-grained sandstone with low water content usually has high resistivity (59).

Grain Size Measurements. The cores were split in the lab and scanned for color reflectance and magnetic susceptibility using Geoteck multi-sensor core logger. Powder samples were taken at 2-cm intervals for grain size measurements after the removal of organic matter and carbonate with 30% hydrogen peroxide and 6 N hydrochloric acid, respectively. Grain size composition was determined using a Marvin 2000 laser instrument at the Institutional Center for Shared Technologies and Facilities of Institute of Earth Environment, Chinese Academy of Sciences. Replicate analyses (n = 30) on silt clay and fine sand samples indicate that analytical errors for the clay content are less than 2%, implying that abrupt content changes (>5%) can be regarded as robust wetting/drying events.

Sedimentary Facies. Based on changes in logging resistivity, core color, and grain size parameters, the sedimentary facies of the HX core can be subdivided into three sedimentary facies of reworked eolian sediment in the upper 25 m and alternations between Littoral-shallow lake and delta front sedimentary environment between 25 and 512 m (*SI Appendix*, Fig. S1 *B–J*). The characteristics of lithological changes in different sedimentary facies are described as follows: 1) reworked eolian deposits characterized by brownish soil interbedded with fine-grained and well-sorted grayish silt layers (*SI Appendix*, Fig. S2*A*); 2) shallow lake deposits including dark grayish mudstone interbedded with dark brownish siltstone and sandstone (*SI Appendix*, Fig. S2*B*); 3) littoral lake deposits consisting of grayish-yellow argillaceous silt interbedded with brownish-yellow medium-to-fine sand layers (*SI Appendix*, Fig. S2*C*); and 4) delta front deposits dominated by grayish or yellowish medium-to-coarse sand layers (*SI Appendix*, Fig. S2*D*).

Magnetostratigraphy. Cube samples were collected from the split core section at 1-m intervals for thermal and alternating-field demagnetization measurements, respectively. For thermal demagnetization (*SI Appendix*, Fig. S3 *A–C*), the natural remanent magnetization was first measured at room temperature (25 °C) and subsequently heated stepwise between temperatures of 50 °C to 620 °C. After each heating step, the remanent magnetization was measured using a 2G 755 superconducting rock magnetometer with a measurement range of 2×10^{-12} to 2×10^{-4} Am^2 and a sensitivity of 2.0×10^{-12} Am^2. For alternating field demagnetization (*SI Appendix*, Fig. S3 *D–F*), the demagnetization was performed stepwise at field strengths from 2.5 mT to 90 mT. After each demagnetization step, the remanent magnetization was also measured using the superconducting magnetometer in a zero-magnetic field space (background value <150 nT). Principal component analysis was used to perform a least-squares linear fit on the demagnetization data above 20 mT and above 300 °C.

Low-Latitude Insolation. Since the Sun passes the equator twice a year, maximum daily isolation occurs at spring and autumn equinoxes (SE and AE), while the minimum insolation occurs at summer and winter solstices (SS and WS) (33). MSID defined as Max (SE, AE)-Min (SS, WS) exhibits the coexistence of eccentricity (400- and 100-ky) and precession harmonics (11, 5.5-ky) (*SI Appendix*, Fig. S9*A*). Over the past 2 Ma, the magnitude of the MSID at the equator ranged between 40 and 100 W/m^2. The 10.5- and 5.5-ky cycles correspond to half-precession and quarter-precession signals, and their amplitudes are strongly modulated by the 400-ky eccentricity cycle. Bihemispheric MDI is defined as a combination of insolation maxima on Jun 21 at 30 °N and on Dec 21 at 30 °S (*SI Appendix*, Fig. S9*B*), which plays a key role in driving heat and water vapor transport over low-latitude oceans.

Spectral and Wavelet Analyses. The Acycle software was used to address the periodic features of power, evolutionary, and coherency spectra of these proxy records (60). Power intensities of dominant periodicities in these proxies were calculated by the multitaper method. Time-frequency characteristics of the evolution spectrum can be obtained using continuous wavelet transforms of these proxies. The MATLAB codes for our wavelet analyses are available at http://grinsted.github.io/wavelet-coherence. The wavelet analysis is performed with a MATLAB software package (61). To further visualize the amplitude and frequency of suborbital components, the high-frequency (<12-ky) signals of insolation and proxy records were filtered for performing the wavelet transforms (*SI Appendix*, Fig. S7). Cross wavelet spectra can obtain common periodicities in two sequences and reveal their phase relationship (62). All proxy data in this study were linearly interpolated at 200-y intervals for spectral and wavelet analyses.

Transient Simulation. Model results were generated from transient simulation performed for the interval of MIS 13 to 12 using the LOVECLIM model (48). The transient simulation only considers impact of astronomically induced insolation based on the calculations of (63), while the greenhouse gas concentrations and ice volume are fixed to the preindustrial concentrations. The simulation was performed with varying astronomical forcing, constant greenhouse gas concentrations, and fixed ice sheets at the present-day extent in order to investigate the effect of insolation alone. The initial condition of an interglacial simulation is provided by a 2000-y long equilibrium simulation using the astronomical parameters at the starting date and the Greenhouse gas concentrations same as the transient experiment. No acceleration technique was applied to the insolation forcing in order to allow a more realistic representation, especially of the slow response in the climate system such as ocean circulations and deep-sea temperature.

Data, Materials, and Software Availability. All relevant data that support the findings of this research can be downloaded from the East Asian Paleoenvironmental Science Database (https://doi.org/10.12262/IEECAS.EAPSD2025003) (64).

ACKNOWLEDGMENTS. We thank Y. Hao, H. Fan, Y. Liu, H. Zhang, Y. Long, H. Wang, M. Zhao, and L. Cheng for laboratory measurements and data analysis. J.B.-G., J. X. are acknowledged for their valuable suggestions on this work. This work was jointly supported by the Natural Science Foundation of China (42494910), Deep Earth probe and Mineral Resources Exploration-National Science and Technology Major Project (2024ZD1001003), International Continental Scientific Drilling Program, the Shandong Province (LSKJ202203300) and the Fonds de la Recherche Scientifique-FNRS (T.0246.23 and T.W019.23).

Author affiliations: [a]State Key Laboratory of Loess Science, Institute of Earth Environment, Chinese Academy of Sciences, Xi'an 710061, China; [b]School of Civil Engineering, Hubei Engineering University, Xiaogan 432000, China; [c]Earth and Climate Research Center, Earth and Life Institute, Université catholique de Louvain, Louvain-la-Neuve 1348, Belgium; [d]Department of Earth, Environmental and Planetary Sciences, Brown University, Providence, RI 02192; [e]Institute of Geological Sciences & Oeschger Centre for Climate Change Research, University of Bern, Bern 63012, Switzerland; [f]School of Biological, Earth and Environmental Sciences, University of New South Wales, Sydney, NSW 2052, Australia; and [g]Open Studio for Oceanic-Continental Climate and Environment Changes, Pilot National Laboratory for Marine Science and Technology, Qingdao 266200, China

1. J. Christian *et al.*, Global distribution, trends, and drivers of flash drought occurrence. *Nat. Commun.* **12**, 6330 (2021).
2. X. Yuan *et al.*, A global transition to flash droughts under climate change. *Science* **380**, 187–191 (2023), 10.1126/science.abn6301.
3. P. Z. Zhang *et al.*, A test of climate, sun, and culture relationships from an 1810-year chinese cave record. *Science* **322**, 940–942 (2008).
4. J. Kennett *et al.*, Drought-induced civil conflict among the ancient Maya. *Nat. Commun.* **13**, 3911 (2022).
5. A. K. Mishra, V. P. Singh, A review of drought concepts. *J. Hydrol.* **391**, 202–216 (2010).
6. V. Masson-Delmotte *et al.*, Eds., *Climate Change: The Physical Science Basis. Contribution of Working Group I to the Sixth Assessment Report of the Intergovernmental Panel on Climate Change* (Cambridge University Press, Cambridge, 2021), pp. 3–32.
7. A. G. Dai, Increasing drought under global warming in observations and models. *Nat. Clim. Change.* **3**, 52–58 (2013).
8. A. Sarhadi, M. C. Ausín, M. P. Wiper, D. Touma, N. S. Diffenbaugh, Multidimensional risk in a nonstationary climate: Joint probability of increasingly severe warm and dry conditions. *Sci. Adv.* **4**, aau3487 (2018).
9. J. Singh *et al.*, Enhanced risk of concurrent regional droughts with increased ENSO variability and warming. *Nat. Clim. Change.* **12**, 163–170 (2022), 10.1038/s41558-021-01276-3.
10. S. Zhou, B. F. Yu, Y. Zhang, Global concurrent climate extremes exacerbated by anthropogenic climate change. *Sci. Adv.* **9**, eabo1638 (2023), 10.1126/sciadv.abo1638.
11. S. Mondal, A. K. Mishra, R. Leung, B. Cook, Global droughts connected by linkages between drought hubs. *Nat. Commun.* **14**, 144 (2023).
12. R. H. Huang, J. L. Chen, G. Huang, Characteristics and variations of the East Asian monsoon system and its impacts on climate disasters in China. *Adv. Atmos. Sci.* **24**, 993–1023 (2007).
13. K. M. Cobb, C. D. Charles, R. L. Edwards, H. Cheng, M. Kastner, El Niño/Southern Oscillation and tropical Pacific climate during the last millennium. *Nature* **424**, 271–276 (2003).
14. Y. Liu *et al.*, Recent enhancement of central Pacific El Niño variability relative to the last eight centuries. *Nat. Commun.* **8**, 15386 (2017), 10.1038/ncomms15386.
15. W. J. Cai *et al.*, Anthropogenic impacts on twentieth-century ENSO variability changes. *Nat. Rev. Earth Environ.* **4**, 407–418 (2023).
16. W. J. Cai *et al.*, Butterfly effect and a self-modulating El Niño response to global warming. *Nature* **585**, 68–73 (2020).
17. Z. S. An *et al.*, Global monsoon dynamics and climate change. *Annu. Rev. Earth Planet. Sci.* **43**, 29–77 (2015).
18. P. X. Wang *et al.*, The global monsoon across time scales, mechanisms and outstanding issues. *Earth Sci. Rev.* **174**, 84–121 (2017).
19. Z. M. Jian *et al.*, Half-precessional cycle of thermocline temperature in the western equatorial Pacific and its bihemispheric dynamics. *Proc. Natl. Acad. Sci. U.S.A.* **117**, 7044–7051 (2020).
20. J. F. McManus, D. E. Oppo, J. L. Cullen, A 0.5-million-year record of millennial-scale climate variability in the North Atlantic. *Science* **283**, 971–974 (1999).
21. S. Barker *et al.*, Persistent influence of precession on northern ice sheet variability since the early Pleistocene. *Science* **376**, 961–967 (2022).
22. Z. S. An *et al.*, Scientific drilling workshop on the weihe basin drilling Project (WBDP): Cenozoic tectonic–monsoon interactions. *Sci. Drilling* **28**, 63–74 (2020).
23. H. Y. Lu *et al.*, Landform evolution in Asia during the Cenozoic revealed by formation of drainages of the Wei River and Indus River. *Palaeogeogr. Palaeoclimatol. Palaeoecol.* **619**, 1115161 (2023).
24. D. S. Rits *et al.*, Facies analysis of the middle and late quaternary sediment infill of the Northern Weihe Basin, Central China. *J. Quat. Sci.* **31**, 152–165 (2016).
25. E. Kalnay *et al.*, The NCEP/NCAR 40-year reanalysis project. *Bull. Amer. Meteor. Soc.* **77**, 437–472 (1996).
26. P. L. Gibbard, M. J. Head, "The Quaternary period" in *Geologic Timescale 2020*, F. M. Gradstein, J. G. Ogg, M.D. Schmitz, G.M. Ogg, Eds. (Elsevier, 2020), pp. 1217–1255.
27. J. E. T. Channell, B. S. Singer, B. R. Jicha, Timing of quaternary geomagnetic reversals and excursions in volcanic and sedimentary archives. *Quat. Sci. Rev.* **228**, 106114 (2020), 10.1016/j.quascirev.2019.106114.
28. Z. S. An *et al.*, Interplay between the westerlies and Asian summer monsoon recorded in Lake Qinghai sediments since 32 ka. *Sci. Rep.* **2**, 619–622 (2012).
29. J. L. Xiao, J. W. Fan, D. Y. Zhai, R. L. Wen, X. G. Qin, Testing the model for linking grain-size component to lake level status of modern clastic lakes. *Quat. Int.* **355**, 34–43 (2015).
30. T. Westerhold *et al.*, An astronomically dated record of Earth's climate and its predictability over the last 66 million years. *Science* **369**, 1383–1387 (2020).
31. L. E. Lisiecki, M. E. Raymo, A Pliocene-Pleistocene stack of 57 globally distributed benthic $\delta^{18}O$ records. *Paleoceanography* **20**, PA1003 (2005).
32. D. A. Hodell, J. E. T. Channell, Mode transitions in Northern Hemisphere glaciation: Co-evolution of millennial and orbital variability in Quaternary climate. *Clim. Past.* **12**, 1805–1828 (2016).
33. A. Berger, M. F. Loutre, J. L. Melice, Equatorial insolation: From precession harmonics to eccentricity frequencies. *Clim. Past* **2**, 131–136 (2006).
34. Y. Zhao *et al.*, Evolution of vegetation and climate variability on the Tibetan Plateau over the past 1.74 million years. *Sci. Adv.* **6**, eeay6193 (2020).
35. M. Melles *et al.*, 2.8 million years of arctic climate change from lake el'gygytgyn. *Science* **337**, 315–320 (2012).
36. Z. S. An *et al.*, Glacial–interglacial Indian summer monsoon dynamics. *Science* **333**, 719–723 (2011).
37. Y. Wang *et al.*, Tropical forcing orbital-scale precipitation variations revealed by a maar lake record in South China. *Clim. Dyn.* **58**, 2269–2289 (2022).
38. B. D. A. Naafs, J. Hefter, R. Stein, Millennial-scale ice rafting events and Hudson Strait Heinrich(-like) events during the late Pliocene and Pleistocene: A review. *Quat. Sci. Rev.* **80**, 1–28 (2013).
39. S. Barker *et al.*, Strengthening Atlantic inflow across the mid-Pleistocene transition. *Paleoceanogr. Paleoclimatol.* **36**, e2020PA004200 (2021), 10.1029/2020PA004200.
40. Y. B. Sun *et al.*, Persistent orbital influence on millennial climate variability through the Pleistocene. *Nat. Geosci.* **14**, 812–818 (2021).
41. D. A. Hodell *et al.*, A 1.5-million-year record of orbital and millennial climate variability in the North Atlantic. *Clim. Past.* **19**, 607–636 (2023).
42. A. C. Clement, L. C. Peterson, Mechanisms of abrupt climate change of the last glacial period. *Rev. Geophys.* **46**, RG4002 (2008).
43. X. Zhang *et al.*, Direct astronomical influence on abrupt climate variability. *Nat. Geosci.* **14**, 819–826 (2021), 10.1038/s41561-021-00846-6.
44. Q. Z. Yin, Z. P. Wu, A. Berger, H. Goosse, D. Hodell, Insolation triggered abrupt weakening of Atlantic circulation at the end of interglacials. *Science* **373**, 1035–1040 (2021).
45. A. McIntyre, B. Molfinot, Forcing of atlantic equatorial and subpolar millennial cycles by precession. *Science* **274**, 1867–1870 (1996).
46. Z. P. Wu, Q. Z. Yin, A. Berger, Z. T. Guo, Forcing mechanisms of the half-precession cycle in the western equatorial Pacific temperature. *Nat. Commun.* **16**, 1841 (2025).
47. Z. T. Guo, X. Zhou, H. B. Wu, Glacial-interglacial water cycle, global monsoon and atmospheric methane changes. *Clim. Dyn.* **39**, 1073–1092 (2012).
48. Z. P. Wu, Q. Z. Yin, Z. T. Guo, A. Berger, Hemisphere differences in response of sea surface temperature and sea ice to precession and obliquity. *Global Planet. Change* **192**, 103223 (2020), 10.1016/j.gloplacha.2020.103223.
49. J. Liu, B. Wang, M. A. Cane, S. Y. Yim, J. Y. Lee, Divergent global precipitation changes induced by natural versus anthropogenic forcing. *Nature* **493**, 656–659 (2013), 10.1038/nature11784.
50. B. Wang *et al.*, Northern hemisphere summer monsoon intensified by mega-ENSO and AMO. *Proc. Natl. Acad. Sci. U.S.A.* **110**, 5347–5352 (2013).
51. Z. Jian *et al.*, Warm pool ocean heat content regulates ocean-continent moisture transport. *Nature* **612**, 92–99 (2022), https://www.nature.com/articles/s41586-022-05302-y.
52. S. C. Clemens, W. L. Prell, D. Murray, G. Shimmield, G. Weedon, Forcing mechanisms of the Indian Ocean monsoon. *Nature* **353**, 720–725 (1991).
53. J. E. Kutzbach, X. Liu, Z. Liu, G. Chen, Simulation of the evolutionary response of global summer monsoons to orbital forcing over the past 280,000 years. *Clim. Dyn.* **30**, 567–579 (2008).
54. T. K. Hagelberg, G. Bond, P. deMenocal, Milankovitch band forcing of sub-Milankovitch climate variability during the Pleistocene. *Paleoceanography* **9**, 545–558 (1994).
55. C. S. M. Turney *et al.*, Millennial and orbital variations of El Niño/Southern Oscillation and high-latitude climate in the last glacial period. *Nature* **428**, 306–310 (2004).
56. X. D. Liu, Z. Y. Liu, J. E. Kutzbach, S. C. Clemens, W. L. Prell, Hemispheric insolation forcing of the Indian and Asian monsoon: Local versus remote impacts. *J. Clim.* **19**, 6195–6208 (2006).
57. A. Berger *et al.*, Interglacials of the last 800,000 years. *Rev. Geophys.* **54**, 162–219 (2016), 10.1002/2015RG000482.
58. Q. Z. Yin, A. Berger, Interglacial analogues of the Holocene and its natural near future. *Quat. Sci. Rev.* **120**, 18–46 (2015).
59. D. Kroon *et al.*, "Coupled Early Pliocene–Middle Miocene Bio-cyclostratigraphy of Site 1006 reveals orbitally induced cyclicity patterns of Great Bahama Bank carbonate production" in *Proceedings of the Ocean Drilling Program, Scientific Results*, P. K. Swart, G. P. Eberli, M. J. Malone, J. F. Sarg, Eds. (2000), pp. 155–166.
60. M. Li, L. Hinnov, L. Kump, Acycle: Time-series analysis software for paleoclimate research and education. *Comput. Geosci.* **127**, 12–22 (2019).
61. J. L. Melice, J. Servain, The tropical Atlantic meridional SST gradient index and its relationship with the SOI, NAO and Southern Ocean. NAO and Southern Ocean. *Clim. Dyn.* **20**, 447–464 (2003).
62. A. Grinsted, J. C. Moore, S. Jevrejeva, Application of the cross wavelet transform and wavelet coherence to geophysical time series. *Nonlin. Proc. Geophys.* **11**, 561–566 (2004).
63. A. Berger, M. F. Loutre, Insolation values for the climate of the last 10 my. *Quat. Sci. Rev.* **10**, 297–317 (1991).
64. Y. Sun, T. Wang. Data from "Suborbtial- and millennial-scale monsoon variability during Pleistocene Interglacials". East Asian Paleoenvironmental Science Database. https://doi.org/10.12262/IEECAS.EAPSD2025003. Deposited 30 April 2025.